Journal of Nuclear Medicine, published on December 18, 2014 as doi:10.2967/jnumed.114.145029

Update in time-of-flight PET imaging

Suleman Surti[1]

[1]Department of Radiology, Perelman School of Medicine, University of Pennsylvania, Philadelphia, PA

Corresponding author and reprint requests:

Suleman Surti, Ph.D.
University of Pennsylvania
Department of Radiology – HUP
404 Blockley Hall
423 Guardian Drive
Philadelphia, PA 19104
Phone: +1 215 662 7214
Fax: +1 215 573 3880
Email: surti@mail.med.upenn.edu

Financial Support:
This work was supported by the National Institutes of Health grant Nos. R01-CA113941 and R01-EB009056.

Short title: Time-of-flight PET

Abstract

Time-of-flight (TOF) PET was initially introduced in the early days of PET. TOF PET scanners developed in the 1980s had limited sensitivity and spatial resolution, operated in 2D mode with septa, and used analytic image reconstruction methods. Current generation of TOF PET scanners have the highest sensitivity and spatial resolution ever achieved in commercial whole-body PET, operate in fully-3D mode, and use iterative reconstruction with full system modeling. Previously, it was shown that TOF provides a gain in image signal-to-noise-ratio (SNR) that is proportional to the square root of the object size divided by the system timing resolution. With oncologic studies being the primary application of PET, more recent work has shown that in modern TOF PET scanners there is an improved trade-off between lesion contrast, image noise, and total imaging time, leading to a combination of improved lesion detectability, reduced scan time or injected dose, and more accurate and precise lesion uptake measurement. The benefit of TOF PET is also higher for heavier patients, which leads to a more uniform clinical performance over all patient sizes.

Key Words: Time-of-Flight PET, Lesion detection, Lesion uptake, scan time.

INTRODUCTION

The signal in PET is produced by the annihilation of an emitted positron with an electron in the surrounding medium or tissue. Positron annihilation leads to the production of two 511 keV photons emitted almost back-to-back that are detected in time coincidence by the surrounding PET detectors to form a line-of-response (LOR). The emission distance along the LOR (d) is determined by $d=c*(t_2-t_1)/2$, where c is the speed of light, and t_1 and t_2 are the arrival times of the two photons (Figure 1A). In conventional PET the difference in arrival time (t_2-t_1) of these two photons is not measured precisely enough to localize the emission point along the LOR. By collecting all possible LORs around the object (full angular coverage) and assuming uniform probability of the emission points lying along the full length of the LORs (and within object boundary), it is mathematically possible to reconstruct the emission object accurately. Knowledge of emission point locations along the LORs is not necessary to reconstruct the emission object. However, by assuming uniform probability of event location along the full LOR length, noise from different emission events gets forward and back projected during image reconstruction over many image voxels leading to increased noise correlation. Hence, the image signal-to-noise ratio (SNR) gets reduced (Figure 1B).

In time-of-flight (TOF) PET the difference in the arrival times (t_2-t_1) of the two photons is measured with high precision that helps localize the emission point along the LOR within a small region of the object (Figure 1C). The uncertainty in this localization is determined by the system coincidence timing resolution, Δt, which is measured as the full-width-half-maximum (fwhm) of the histogram of TOF measurements from a point

source (timing spectrum). The corresponding uncertainty in spatial localization (Δx) along the LOR is given by $\Delta x = c * \Delta t/2$. If Δx is the same or smaller then the detector spatial resolution (around 4-5 mm for modern PET scanners) then in principle image reconstruction is not needed. Typically this spatial localization is an order of magnitude worse than the detector spatial resolution, and hence image reconstruction is still necessary to produce tomographic images. However, during reconstruction, noise from different events is now forward and back projected over only a limited number of image voxels as defined by the spatial uncertainty, leading to reduced noise correlations and improved image SNR (Figure 1D).

HISTORICAL BACKGROUND

Using TOF information to localize the emission point along an LOR was recognized from the very early days (1960s) of PET (*1-3*). However, it was not until the 1980s that the first TOF PET machines were developed for clinical use (*4-9*). The primary application of PET in those days was in cardiology and brain imaging with tracers using short-lived isotopes such as ^{15}O and ^{13}N. Hence, the motivation for developing TOF PET was driven by the need to improve SNR in reconstructed images and reduce random coincidences in the collected data. These early TOF PET systems utilized CsF and later BaF_2 as the scintillators and had system coincidence timing resolution in the range of 450-750 ps. Compared to slower scintillators such as BGO and NaI(Tl) that were being used in Non-TOF PET scanners, both CsF and BaF_2 had poor detection efficiency and low light output. Consequently, system spatial resolution in these early TOF PET systems was poor due to the need to use larger crystals, and the SNR gains due to TOF were not

large enough to compensate for the reduced detector sensitivity. While these TOF PET systems met the early demands of high count-rate brain and cardiac studies, by early 1990s they were superseded by the Non-TOF PET scanners based primarily on BGO and to a lesser extent on NaI(Tl), since the lower detection efficiency overwhelmed the advantage of TOF in these systems. A very good summary of this history is presented by Lewellen (*10*).

PAST ESTIMATES FOR TOF GAIN

With the knowledge that during the forward and back projection steps in image reconstruction noise will be spread over fewer voxels along the LOR (defined by Δx), it was shown previously (*11, 12*) that the effective gain in sensitivity at the center of a uniform cylinder due to TOF information is given by $D/\Delta x$. Figure 2A shows a plot of this gain in sensitivity plotted as a function of timing resolution and for varying object sizes. As the object size increases or timing resolution improves the gain due to TOF PET increases. This derivation of TOF PET is based on the assumption that the histogram for TOF measurements (timing spectrum) from a fixed point source has a uniform distribution with a width equal to the system timing resolution, Δt (or Δx). However, in practice the timing spectrum has a Gaussian shape with tails that spread noise over pixels beyond those defined by Δx. Hence, this sensitivity gain metric is an over-estimate. A more detailed estimation of TOF gain was performed by Tomitani (*13*) which included the effects of filtering during the reconstruction process to arrive at an estimate for TOF gain given by $D/(1.6^* \Delta x)$ under the condition that Δx is greater than or equal to twice the detector spatial resolution. Both these derivations, however, showed that TOF sensitivity

gain is proportional to the object size (D) and inversely proportional to the detector timing resolution (Δt or Δx). These results were also consistent with subsequent evaluations performed in the 1980s (*14, 15*). PET imaging in the 1980s was geared more towards high activity, or high count-rate, brain and cardiac studies where random coincidences are a significant component of the collected data. It was originally suggested (*16*) and subsequently shown (*17*) through uniform cylinder measurements that the sensitivity gain due to TOF as defined by the above formulas for low activity levels also increases as a function of activity level due to the reduced impact of random coincidences in TOF images. Figure 2B (*17*) shows a plot of measured gain due to TOF as a function of activity concentration in a uniform cylinder. The TOF gain was measured as ratio of the variance in reconstructed Non-TOF and TOF images. As activity concentration and hence randoms fraction increases, TOF gain also increases.

NEW GENERATION OF TOF PET SCANNERS

The advent of lutetium oxy-orthosilicate (LSO) crystal in mid to late 1990s led to the recognition that a new class of very fast scintillators existed that could provide a combination of high light output and high stopping efficiency for 511 keV photons. The immediate advantage of a crystal like LSO over BGO was the ability to achieve high count-rate capability, reduce random coincidence rate with the use of a tight coincidence timing window ($\leq \pm$ 3 ns), improve system spatial resolution, and provide maximum benefits from fully-3D imaging (without septa). In addition, it was also recognized that the combination of high light output and short decay time of LSO provides good timing resolution necessary for TOF PET (*18, 19*). In 2005, early results from a commercial

LSO PET system showed a system timing resolution of 1.2 ns achieved with photomultiplier tubes (PMTs) and electronics that were not optimized for TOF imaging (*20*). Subsequently, the first commercial TOF PET scanner using lutetium-yttrium oxy-orthosilicate (LYSO, another crystal with properties similar to LSO) was introduced with a timing resolution of 585 ps (*21*). Since then all three commercial manufacturers have introduced some version of an LSO or LYSO based TOF PET scanner with system timing resolution in the 450-500 ps range. Compared to the first generation TOF PET scanners from the 1980s, these systems do not compromise system sensitivity or spatial resolution. In fact the Non-TOF performance of these scanners is the highest that has been achieved historically. Also, compared to the first generation systems, the current TOF scanners operate in fully-3D mode because of good system energy resolution and the ability to correct and reconstruct large data sets due to advances in computer hardware. The new systems also benefit from the development of new, small, and cost-effective PMTs with good timing performance. Developments in electronics with new ASIC and FPGA designs have also led to more stable timing performance of these new systems over extended time periods. Finally, image reconstruction techniques have developed significantly from the 1980s where primarily analytical algorithms such as most-likely position (MLP) (*11*) and confidence weighted (CW) backprojection (*11, 13, 22*) were used for image generation. In recent years there have been significant developments in iterative list-mode reconstruction algorithms with full system modeling, including TOF kernel, included in the reconstruction (*23-28*). In combination with faster CPUs and parallelization of reconstruction algorithms, these techniques have become practical and feasible for clinical use. While all these technical advancements have led to

significant improvements in TOF PET technology and made it a necessary component of all modern PET scanners, the growth of ^{18}F-FDG PET imaging in oncology is now the primary driver for most advancements in PET technology.

Gain in Image SNR from fully-3D TOF PET

The recent introduction of fully-3D TOF PET scanners led to an initial focus on estimating the gain in sensitivity or SNR due to TOF information along lines similar to what was done previously in the 1980s. However, the physical noise equivalent counts (NEC) metric was now used to better estimate the impact of increased true, random and scatter coincidences in fully-3D PET. The NEC metric was developed as a physical surrogate to estimate the image SNR (NEC = SNR^2) at the center of a uniform cylinder after taking into account the contributions of not only true coincidences but also scatter and random coincidences (*29*). NEC, therefore, represents the effective sensitivity of a PET scanner. For TOF PET the NEC metric was extended (*30*) to show that,

$$NEC_{TOF} = \left(\frac{D}{\Delta x}\right) \bullet \left(\frac{T + Sc + \beta R}{T + Sc + \beta^2 R}\right) \bullet NEC_{Non-TOF} \qquad \text{(Eq. 1)}$$

where $\beta = D / D_{FOV}$, D_{FOV} is the diameter of the imaging FOV, and T, Sc and R are the number of true, scatter, and random coincidences. As can be seen, this formulation of NEC is consistent with the past observation of the gain in sensitivity from TOF being proportional to the object size, inversely proportional to the timing resolution, and increasing as the relative number of random coincidences increased. This derivation of gain in NEC due to TOF information was verified in a scanner with a 1.2 ns timing resolution (*30*) (with some limitations at low activity levels) when using a special

implementation of TOF filtered backprojection reconstruction algorithm (*20*). While this formulation of NEC gives a reasonable starting point for understanding the potential benefits of TOF, the effect of iterative image reconstruction especially the choice of number of iterations to use, and data correction schemes as implemented on clinical scanners is not captured by this metric. Also, better understanding the impact of TOF in clinical studies with non-uniform activity distribution in patients requires the use of task-dependent metrics that are closer to the clinical process of patient disease evaluation. However, the multi-parameter effect on the resultant images and the non-linear characteristics of these task-dependent metrics makes it impossible to assign a single gain factor in the resultant images due to TOF information.

STUDIES DEMONSTRATING BENEFIT OF MODERN TOF PET SCANNERS IN CLINICALLY RELEVANT IMAGING TASKS

Lesion uptake measurement is a common task performed on ^{18}F-FDG images in order to distinguish between benign and malignant tumors, as well as to determine disease progression during therapy. With iterative reconstruction, each additional iteration of the algorithm brings the lesion uptake measurement closer to convergence but with the penalty of increased noise in the image. Investigations performed over the last decade using both physical phantoms (*20, 31-37*) as well as clinical patient studies (*33, 36*) have shown that with TOF imaging the lesion uptake or contrast recovery coefficient (CRC) converges faster or requires fewer iterations to achieve the maximal contrast. Figure 3A (*33*) shows TOF and Non-TOF images reconstructed from the same data set for a 35-cm diameter lesion phantom as a function of iteration number. From this set of images it is

clearly observed that the smallest hot sphere (10 mm in diameter) is easily visible even after 1 iteration (due to fast recovery of lesion uptake). For Non-TOF images, even after 20 iterations the 10 mm sphere is not clearly visible while the noise in the image is significantly enhanced. Figure 3B (*33*) shows TOF (5 iterations) and Non-TOF (10 iterations) images as a function of varying scan times. The choice of the iteration number was based on the relative convergence of the two image sets with very little increase in lesion uptake with more iterations. From this image we observe that for the Non-TOF image the 10 mm sphere is not visible even after a 5 min scan while we need scan time of > 2 min to see the 13 mm diameter sphere. With TOF all lesions are visible after scan times of 2 min. Figure 3C (*33*) shows lesion contrast recovery coefficient (CRC) plotted as a function of image noise for the 13 mm diameter sphere. For the same scan time and noise, TOF leads to higher CRC. For similar CRC, Non-TOF image has higher noise and increasing the scan time from 2 min to 5 min still does not lead to a noise level similar to the 2 min TOF image, indicating the potential to reduce scan time with TOF imaging. Since clinical studies are performed to achieve a certain fixed level of image noise for either TOF or Non-TOF data, these phantom studies indicate that in patients TOF imaging should lead to increased lesion uptake measurements. In Figure 3D (*33*) we show results from a five patient study showing the average gain in contrast due to TOF information for several lesions within each patient. The TOF and Non-TOF images were chosen for a fixed number of iterations number over all patients and which gave similar pixel-to-pixel noise within the liver. As seen in the phantom studies, TOF leads to a gain in lesion contrast measurement with a trend towards higher gain in larger patients.

Lesion Detectability in a Uniform Background Phantom

As described above, the interplay between image noise (function of scan time and number of iterations of reconstruction algorithm) and lesion uptake (or CRC) measurement has a direct impact on lesion detectability in a PET image, especially in the case of TOF data which has a faster CRC convergence. An early simulation study (*31*) using a numerical observer (non-prewhitening matched filter signal-to-noise ratio, or NPW SNR) showed a gain in small lesion (10 mm diameter) detectability with TOF PET in a uniform cylinder. The NPW SNR metric showed a non-linear increase as a function of count statistics and timing resolution and the gains were proportional (but less) than the simplified estimate of $(D/\Delta x)^{1/2}$. These results were subsequently verified experimentally (*34*). Figure 4 (*34*) shows sample reconstructed images from this study after a 5 min scan, and the NPW SNR results as a function of scan time. NPW SNR is always higher for TOF images and the relative gain increases with scan time.

Lesion Detectability in a Non-uniform, Anthropomorphic Phantom

A simplification in the above lesion detection studies was the task of detecting lesions at a fixed known position (signal known exactly, or SKE) in a uniform background. Clinically, patient habitus is non-uniform while the presence of statistical noise in PET data significantly affects the ability to detect lesions at previously unknown positions. Working towards this direction, a detailed study was performed by Kadrmas, et al. (*38*) for detecting focal lesion hot spots in an anthropomorphic phantom. Using numerical as well as untrained (non-clinical), human observers their results showed a significant gain in the area under the LROC curve (ALROC) after including TOF information in image

reconstruction. The ALROC metric represents the probability that an observer correctly identifies the presence and location of a lesion in the image and hence represents a more clinically realistic measure to quantify the benefit of TOF PET. A follow-up study (*39*), utilizing numerical observers and a larger anthropomorphic phantom showed that with TOF PET scan time could be reduced by as much as 40% with TOF to achieve similar ALROC as in Non-TOF PET.

Lesion Detectability in Clinical Patients

Finally, a study utilizing 100 normal patient data sets was developed where synthetic, measured lesion data were introduced in the list data from the scanner followed by image reconstruction (*40, 41*). Lesions were added in the lung and liver regions of the patients. First part of this study utilized a numerical observer to calculate lesion detectability for a SKE task. Results from this work (*40*) showed a gain in lesion detectability from TOF information over all patient sizes, lesion contrast, and scan times and were used to set up a human observer study with a selected sub-section of the images. The second part of this study (*41*) utilized human observers (combination of clinicians as well as a non-clinician) to read the images and determine the presence (and location) or absence of a lesion. Figure 5A (*41*) shows sample reconstructed images for a patient (BMI of 28.4) with a lesion inserted in the liver. Longer scan time and TOF imaging lead to a qualitative improvement in lesion detection. Figure 5B (*41*) shows summary results for ALROC results for the liver lesions. This study showed that while overall, heavy patients have lower ALROC values compared to light patients, longer scans (3 min per bed position) lead to improved ALROC values. Also, TOF information leads to improved performance

with a bigger benefit in heavy patients. Hence, in heavy patients the use of TOF information together with longer scan times (3 min per bed position) led to ALROC values that were similar to those achieved in light patients, indicating a more uniform performance due to TOF imaging over different patient habitus.

Accuracy and Precision of Lesion Uptake Measurement in Patients

The technique of synthetically added lesions to normal patient data before image reconstruction has also been employed to quantitatively measure the benefit of TOF imaging on the accuracy and precision of lesion uptake measurements in patients (*42*, *43*). This study was performed on a research whole-body scanner with 375ps timing resolution (*44*). Six normal volunteers were imaged and 10 mm diameter spheres with 10:1 uptake ratio relative to whole-body activity concentration were inserted in the lung and liver regions. Figure 6 (*43*) shows the summary results from this study. Normalized uptake value (NUV) is the average lesion uptake normalized to the whole-body uptake and should equal 10 for full uptake recovery. In this study the number of TOF and Non-TOF reconstruction algorithm iterations were fixed to achieve similar image noise. As shown in Figure 6A the average NUV was higher with TOF versus Non-TOF, and is higher overall in the liver versus lung lesions. However the ratio of NUV in lung to liver is less with TOF (1.48 versus 1.85). In Figure 6B we also see the variability in the NUV values is always lower with TOF – over different replicates of the same lesion, over different lesions within the same organ, and over different subjects. The reduced NUV variability indicates increased precision and higher confidence in lesion uptake measurement for routine clinical studies.

OTHER BENEFITS OF TOF INFORMATION IN PET IMAGING STUDIES

Non-TOF PET data acquired in 2D mode (with septa) collects all angular projections necessary to tomographically reconstruct the entire 3D patient volume. Fully-3D PET (no septa) was previously recognized to provide redundant information that helped improve the statistical noise properties of the reconstructed PET image. Similarly, TOF information with good timing resolution provides additional information that helps provide consistency requirements in the image reconstruction process. Hence, as recognized by several groups (*45, 46*) TOF PET images are more robust, being less sensitive to errors in data correction techniques (such as normalization, scatter and attenuation correction) and leading to good image quality despite these limitations. Figure 7 (*46*) shows Non-TOF and TOF PET images from a thorax phantom study where the transmission image is offset from the emission image (Figure 7A), inconsistent normalization data are used for image reconstruction (Figure 7B), and no scatter correction is applied (Figure 7C). These images show that TOF PET imaging is less sensitive to errors in data correction and can provide benefits in certain clinical imaging scenarios. For instance, patient motion or truncation of attenuation map (from CT) will affect not only attenuation correction but also the scatter estimate. Precise TOF information will be useful in these scenarios to produce meaningful clinical images.

Another potential benefit of TOF information is in the area of limited angle reconstruction where a full PET detector ring may not be available or be impractical. This

application has been evaluated though simulation studies for clinical whole-body PET where the cost of a PET scanner can potentially be reduced (*47*), dedicated breast PET where two PET detectors can be used to image the breast in a flexible geometry (*48, 49*), and proton therapy where in-beam PET can be used to monitor the proton beam range (*50, 51*).

FUTURE APPLICATION IN LOW-COUNT IMAGING SCENARIOS

Currently the benefits of improved imaging performance of TOF PET in the clinic have been utilized mainly to reduce the patient imaging times and/or improve image quality in heavy patients. Routine clinical ^{18}F-FDG imaging involves injection of 10-15 mCi of the radiotracer followed by patient imaging times ranging from 0.5-2 min per bed position depending on the patient size. Improved image quality from TOF PET could be utilized in these routine clinical situations to perform respiratory gating with a reduced penalty of noise in the image due to a loss of counts. Another area of application of PET lies in monitoring disease progression or the assessment of tumor response to therapy. Traditional techniques such as CT and MRI depend on macroscopic anatomical or morphological changes in the tumor size to perform these tasks. By providing functional information, PET imaging can lead to an early disease assessment and help in reducing patient morbidity from drug toxicity as well as reducing treatment costs. Multiple PET scans are needed in this scenario and injected patient dose becomes an important consideration. By using TOF PET to reduce injected dose, one could potentially maintain good imaging performance with moderate imaging times in order to perform the multiple PET scans needed for this application. Finally, immuno-PET is a rapidly growing area

that utilizes long-lived positron-emitting radio-isotopes to label and track the localization of monoclonal antibodies (*52*). New studies using ^{89}Zr and ^{124}I based radiotracers to identify and determine optimal dosage for therapeutic targets such as HER2 in breast cancer (*53*) perform imaging at 2-4 days after injection of small (a few mCi) doses of radiotracer. TOF PET with moderate imaging times can provide accurate, quantitative images for these applications (*54*).

SUMMARY

In the 1980s, a first generation of TOF PET scanners were developed and demonstrated improved SNR in the reconstructed images compared to the same scanners when operating in Non-TOF mode. Limited sensitivity and spatial resolution of these systems led to a migration of commercial whole-body PET scanners towards higher sensitivity, Non-TOF systems with improved spatial resolution, and eventually even higher sensitivity with the introduction of fully-3D imaging. After the development of fast, new scintillators, which not only improved on the Non-TOF performance of PET but also provided TOF capability, the last decade has seen a re-introduction of TOF PET as a commercial product with two major technical differences from the previous generation of TOF PET scanners: the new TOF PET scanners operate in fully-3D mode without septa and image reconstruction algorithms are iterative 3D algorithms as opposed to being 2D analytic algorithms. Consequently, the previous measures for TOF gain estimated simply as a reduction in noise (or increase in sensitivity or SNR) become harder to apply since the impact of scatter and random coincidences changes, and the choice of number of iterations used for image reconstruction affects the contrast and noise in the image in a

non-linear manner. Together with the primary clinical application of PET being in oncology, this has led to use of more clinically relevant (and non-linear) metrics to evaluate the gains in image quality due to TOF information. These studies have demonstrated improved lesion detection and quantitative performance for routine clinical ^{18}F-FDG imaging tasks, leading to shorter imaging times and a more uniform performance over varying patient habitus. Due to the non-linear behavior of these metrics assigning a value to the gain in image quality due to TOF information is not possible, but in agreement with the past work the impact of TOF information is higher for larger patients and increases with improved timing resolution. In smaller patients, while the benefit due to TOF information may not be significant, one could consider using shorter scan times to achieve good quality images. The robustness of TOF image reconstruction could also be beneficial for all patients where small errors in data corrections or patient motion will have a reduced impact on the reconstructed image. As a result, TOF PET has become a standard technology in almost all commercial systems and is used routinely for clinical and research studies.

From a hardware perspective, while achieving good timing resolution requires paying some attention to the electronics design as well as the type of PMT being used, the technical goals are relatively easy to achieve without a significant increase in the cost of the system. The large size of TOF PET data and the need to reconstruct images efficiently could be considered to be a drawback in routinely using TOF PET, but advances in computational hardware has already made TOF PET practical and future developments will only reduce the complexity of this task. Development of new scintillators that

improve on the performance of existing systems can lead to further improvements in the system timing resolution. For example, lanthanum bromide ($LaBr_3$) is a scintillator that has been used to develop a research whole-body PET scanner with system timing resolution of 375 ps (*44*). Compared to lutetium-based scintillators (LSO or LYSO), $LaBr_3$ has a lower detection efficiency but very high light output which leads to improved timing and energy resolution. Alternately, the used of new co-dopants such as Ca or Mg, has been shown to increase the light output and shorten the decay time of LSO (*55*), and leads to improved timing resolution over standard LSO (*56*). In addition to new scintillators, the choice of photo-detector also has a big impact on the detector timing resolution. PMTs have fast timing performance and have been used in all commercial TOF PET scanners until recently. Due to PMT size limitations PET detectors typically use some form of light sharing method to decode crystals which are generally about a factor of ten smaller in size than the PMT. New silicon photomultiplier tubes (SiPMs) provide fast timing performance with very small detectors that allow direct 1-1 coupling to the scintillator. Since minimal or no light sharing methods are used here, the intrinsic timing resolution of PET systems using these photo-detectors will be lower. A commercial whole-body PET/CT has already been developed with a reported system timing resolution of 309 ps (*57*). An added advantage of the SiPMs is their ability to operate within a magnetic field. With the current introduction of PET/MR scanners, SiPMs provide the only technological solution to achieve TOF PET in a simultaneous PET/MR system. A prototype, simultaneous TOF PET/MR scanner using this technology has also recently been developed and shown to achieve 390 ps timing resolution (*58*). Hence, in the near future TOF PET systems with 300-400 ps timing resolution will

become widespread using currently available scintillators, and it is conceivable to reach even higher performance with new scintillators such as $LaBr_3$ or Ca co-doped LSO.

In the future, TOF PET may play an important role in situations that require low dose, serial ^{18}F-FDG imaging of patients, as well as imaging with long-lived radio-isotopes for targeted therapy. These applications require low noise images with reduced counts that are also quantitatively accurate – an area where TOF PET provides significant advantages. Further utilization of PET in these areas will benefit with ongoing instrumentation efforts to provide further improvements in system timing resolution, as well as more accurate data correction and image reconstruction algorithms.

ACKNOWLEDGMENTS

This work was supported by the National Institutes of Health grant Nos. R01-CA113941 and R01-EB009056.

REFERENCES

1. Anger HO. Survey of Radioisotope Cameras. *ISA Trans.* 1966;5:311.

2. Brownell GL, Burnham CA, Wilensky S, Aronow S, Kazemi H, Streider D. New developments in positron scintigraphy and the application of cyclotron produced positron emitters. *Medical Radioisotope Scintigraphy.* Vol 1. Vienna, Austria: IAEA (Proceedings Series); 1969:163-176.

3. Budinger TF. Instrumentation trends in nuclear medicine. *Semin Nucl Med.* 1977;7:285-297.

4. Ter-Pogossian MM, Ficke DC, Hood JT, Sr., Yamamoto M, Mullani NA. PETT VI: A positron emission tomograph utilizing cesium fluoride scintillation detectors. *J Comput Assist Tomogr.* 1982;6:125-133.

5. Ter-Pogossian M, Ficke D, Yamamoto M, JT H. Super PETT I: A Positron Emission Tomograph utilizing photon time-of-flight information. *IEEE Trans Med Imag.* 1982;M1-1:179-187.

6. Gariod R, Allemand R, Cormoreche E, Laval M, Moszynski M. The "LETI" positron tomograph architecture and time-of-flight improvements. Paper presented at: Proceedings of IEEE Workshop on Time-of-Flight Emission Tomography, 1982; Washington University, St. Louis, MO.

7. Wong WH, Mullani NA, Philippe EA, et al. Performance characteristics of the University of Texas TOF PET-I Camera. *J Nucl Med.* 1984;25:46-47.

8. Lewellen TK, Bice AN, Harrison RL, Pencke MD, Link JM. Performance measurements of the SP3000/UW time-of-flight positron emission tomograph. *IEEE Trans Nucl Sci.* 1988;35:665-669.

9. Mazoyer B, Trebossen R, Schoukroun C, et al. Physical characteristics of TTV03, a new high spatial resolution time-of-tlight positron tomograph. *IEEE Trans Nucl Sci.* 1990;37:778-782.

10. Lewellen TK. Time-of-flight PET. *Semin Nucl Med.* 1998;28:268 - 275.

11. Snyder DL, Thomas LJ, Terpogossian MM. A mathematical model for positron emission tomography systems having time-of-flight measurements. *IEEE Trans Nucl Sci.* 1981;28:3575-3583.

12. Budinger TF. Time-of-flight positron emission tomography - status relative to conventional PET. *J Nucl Med.* 1983;24:73-76.

13. Tomitani T. Image reconstruction and noise evaluation in photon time-of-flight assisted positron emission tomography. *IEEE Trans Nucl Sci.* 1981;28:4582-4589.

14. Snyder DL, Politte DG. Image reconstruction from list-mode data in an emission tomography system having time-of-flight measurements. *IEEE Trans Nucl Sci.* 1983;30:1843-1849.

15. Wong WH, Mullani NA, Philippe EA, Hartz R, Gould KL. Image improvement and design optimization of the time-of-flight PET. *J Nucl Med.* 1983;24:52-60.

16. Yamamoto M, Hoffman GR, Ficke DC, Ter-Pogossian MM. Imaging algorithm and image quality in time-of-flight assisted positron computed tomography: Super PETT I. Paper presented at: Proceedings of IEEE Workshop on Time-of-Flight Emission Tomography, 1982; Washington University, St. Louis, MO.

17. Yamamoto M, Ficke DC, Ter-Pogossian MM. Experimental assessment of the gain achieved by the utilization of time-of-flight information in a positron emission tomograph (Super PETT I). *IEEE Trans Med Imag.* 1982;1:187-192.

18. Moses WW, Derenzo SE. Prospects for time-of-flight PET using LSO scintillator. *IEEE Trans Nucl Sci.* 1999;46:474-478.

19. Moses WW. Time of flight in PET revisited. *IEEE Trans Nucl Sci.* 2003;50:1325-1330.

20. Conti M, Bendriem B, Casey M, et al. First experimental results of time-of-flight reconstruction on an LSO PET scanner. *Phys Med Biol.* 2005;50:4507-4526.

21. Surti S, Karp J, Werner M, Kolthammer J. Imaging performance of an LYSO-based TOF PET scanner. *J Nucl Med.* 2006;47:54P.

22. Snyder DL. Some noise comparisons of data collection arrays for emission tomography systems having time-of-flight measurements. *IEEE Trans Nucl Sci.* 1982;29:1029-1033.

23. Reader AJ, Erlandsson K, Flower MA, Ott RJ. Fast accurate iterative reconstruction for low-statistics positron volume imaging. *Phys Med Biol.* 1998;43:835-846.

24. Parra L, Barrett HH. List-mode likelihood: EM algorithm and image quality estimation demonstrated on 2-D PET. *IEEE Trans Med Imag.* 1998;17:228 - 235.

25. Huesman RH, Klein GJ, Moses WW, Qi JY, Reutter BW, Virador PRG. List-mode maximum-likelihood reconstruction applied to positron emission mammography (PEM) with irregular sampling. *IEEE Trans Med Imag.* 2000;19:532-537.

26. Kimdon JA, Qi J, Moses WW. Effect of random and scatter fractions in variance reduction using time-of-flight information. Paper presented at: 2003 IEEE Nuclear Science Symposium and Medical Imaging Conference, 2003; Portland, OR.

27. Popescu LM. Iterative image reconstruction using geometrically ordered subsets with list-mode data. Paper presented at: 2004 IEEE Nuclear Science Symposium and Medical Imaging Conference, 2004; Rome, Italy.

28. Popescu LM, Lewitt RM. Tracing through a grid of blobs. Paper presented at: 2004 IEEE Nuclear Science Symposium and Medical Imaging Conference, 2004; Rome, Italy.

29. Strother SC, Casey ME, Hoffman EJ. Measuring PET scanner sensitivity: Relating count rates to image signal-to-noise ratios using noise equivalent counts. *IEEE Trans Nucl Sci.* 1990;37:783-788.

30. Conti M. Effect of randoms on signal-to-noise ratio in TOF PET. *IEEE Trans Nucl Sci.* 2006;53:1188-1193.

31. Surti S, Karp JS, Popescu LA, Daube-Witherspoon ME, Werner M. Investigation of time-of-flight benefit for fully 3-D PET. *IEEE Trans Med Imag.* 2006;25:529-538.

32. Surti S, Kuhn A, Werner ME, Perkins AE, Kolthammer J, Karp JS. Performance of Philips Gemini TF PET/CT scanner with special consideration for its time-of-flight imaging capabilities. *J Nucl Med.* 2007;48:471-480.

33. Karp JS, Surti S, Daube-Witherspoon ME, Muehllehner G. Benefit of time-of-flight in PET: experimental and clinical results. *J Nucl Med.* 2008;49:462-470.

34. Surti S, Karp JS. Experimental evaluation of a simple lesion detection task with time-of-flight PET. *Phys Med Biol.* 2009;54:373-384.

35. Vandenberghe S, Karp J, Lemahieu I. Influence of TOF resolution on object dependent convergence in iterative listmode MLEM. *J Nucl Med.* 2006;47:58P.

36. Lois C, Jakoby BW, Long MJ, et al. An assessment of the impact of incorporating time-of-flight information into clinical PET/CT imaging. *J Nucl Med.* 2010;51:237-245.

37. Kolthammer JA, Tang J, Perkins AE, Muzic RF. Time-of-flight precision and PET image accuracy. Paper presented at: 2010 IEEE Nuclear Science Symposium Conference Record, 2010; Knoxville, TN.

38. Kadrmas DJ, Casey ME, Conti M, Jakoby BW, Lois C, Townsend DW. Impact of time-of-flight on PET tumor detection. *J Nucl Med.* 2009;50:1315-1323.

39. Kadrmas DJ, Oktay MB, Casey ME, Hamill JJ. Effect of scan time on oncologic lesion detection in whole-body PET. *IEEE Trans Nucl Sci.* 2012;59:1940-1947.

40. El Fakhri G, Surti S, Trott CM, Scheuermann J, Karp JS. Improvement in lesion detection with whole-body oncologic TOF-PET. *J Nucl Med.* 2011;52:347-353.

41. Surti S, Scheuermann J, El Fakhri G, et al. Impact of TOF PET on whole-body oncologic studies: a human observer detection and localization study. *J Nucl Med.* 2011;52:712-719.

42. Surti S, Perkins AE, Clementel E, Daube-Witherspoon ME, Karp JS. Impact of TOF PET on variability of lesion uptake estimation. Paper presented at: World Molecular Imaging Conference, 2010; Kyoto, Japan.

43. Daube-Witherspoon ME, Surti S, Perkins AE, Karp JS. Determination of accuracy and precision of lesion uptake measurements in human subjects with time-of-flight PET. *J Nucl Med.* 2014;55:602-607.

44. Daube-Witherspoon ME, Surti S, Perkins AE, Kyba CCM, Wiener RI, Karp JS. Imaging Performance of a $LaBr_3$-based Time-of-Flight PET Scanner. *Phys Med Biol.* 2010;55:45-64.

45. Turkington TG, Wilson JM. Attenuation artifacts and time-of-flight PET. Paper presented at: 2009 IEEE Nuclear Science Symposium and Medical Imaging Conference, 2009; Orlando, FL.

46. Conti M. Why is TOF PET reconstruction a more robust method in the presence of inconsistent data? *Phys Med Biol.* 2011;56:155-168.

47. Vandenberghe S, Lemahieu I. System characteristics of simulated limited angle TOF PET. *Nucl Instr Meth (A).* 2007;571:480-483.

48. Surti S, Karp JS. Design considerations for a limited angle, dedicated breast, TOF PET scanner. *Phys Med Biol.* 2008;53:2911-2921.

49. Lee E, Werner ME, Karp JS, Surti S. Design optimization of a time-of-flight, breast PET scanner. *IEEE Trans Nucl Sci.* 2013;60:1645-1652.

50. Crespo P, Shakirin G, Fiedler F, Enghardt W, Wagner A. Direct time-of-flight for quantitative, real-time in-beam PET: a concept and feasibility study. *Phys Med Biol.* 2007;52:6795-6811.

51. Surti S, Zou W, Daube-Witherspoon ME, McDonough J, Karp JS. Design study of an in-situ PET scanner for use in proton beam therapy *Phys Med Biol.* 2011;56:2667-2685.

52. Wright BD, Lapi SE. Designing the magic bullet? The advancement of immuno-PET into clinical use. *J Nucl Med.* 2013;54:1171-1174.

53. Dijkers ECF, Kosterink JGW, Rademaker AP, et al. Development and characterization of clinical-grade ^{89}Zr-Trastuzumab for HER2/neu immunoPET imaging. *J Nucl Med.* 2009;50:974-981.

54. Surti S, Scheuermann R, Karp JS. Correction technique for cascade gammas in I-124 imaging on a fully-3D, time-of-flight PET scanner. *IEEE Trans Nucl Sci.* 2009:653-660.

55. Spurrier MA, Szupryczynski P, Kan Y, Carey AA, Melcher CL. Effects of Ca^{2+} Co-Doping on the Scintillation Properties of LSO:Ce. *IEEE Trans Nucl Sci.* 2008;55:1178-1182.

56. Conti M, Eriksson L, Rothfuss H, Melcher CL. Comparison of Fast Scintillators With TOF PET Potential. *IEEE Trans Nucl Sci.* 2009;56:926-933.

57. Miller M, Griesmer J, Jordan D, et al. Initial characterization of a prototype digital photon counting PET system. *Society of Nuclear Medicine Annual Meeting Abstracts.* 2014;55:658.

58. Levin C, Glover G, Deller T, McDaniel DL, Peterson W, Maramraju SH. Prototype time-of-flight PET ring integrated with a 3T MRI system for simultaneous whole-body PET/MR imaging. *Society of Nuclear Medicine Annual Meeting Abstracts.* 2013;54:148.

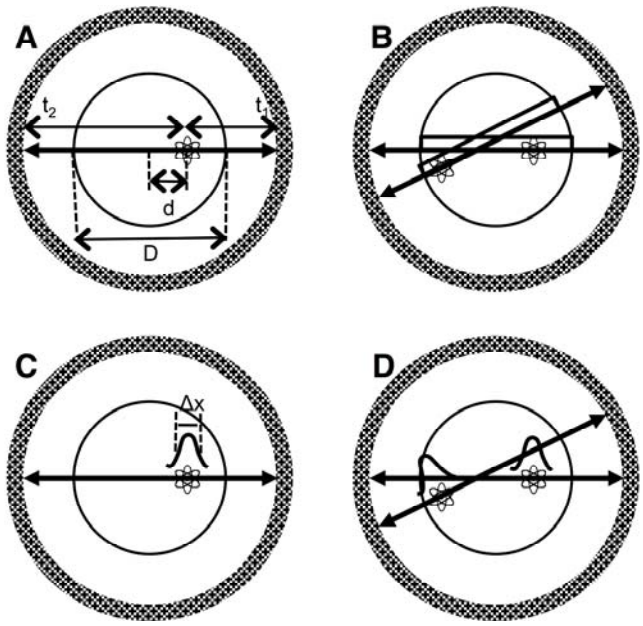

Figure 1. (A) Emission point at a distance d from the center of the scanner within an object of diameter D. The two 511 keV photons are detected in coincidence at times t_1 and t_2. (B) Without precise TOF measurement a uniform probability along the LOR within the object is assumed for each emission point, leading to noise correlations over a portion of image space between the two events as shown here. (C) With TOF information the position of the emission point is localized along the LOR with a precision that is defined by a Gaussian distribution of width Δx. (D) Better localization of the two emission events along their individual LORs leads to reduced (or no, as shown here) noise correlation of the events in image space during image reconstruction.

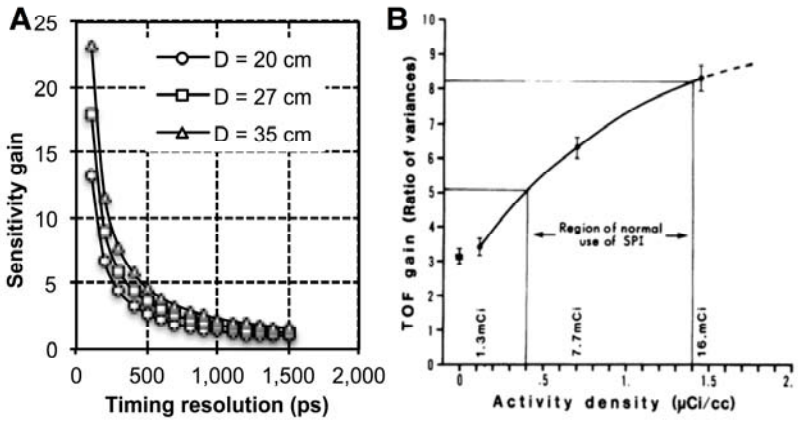

Figure 2. (A) Gain in sensitivity as defined by D/Δx plotted as a function of timing resolution for cylindrical phantoms with three different diameters. (B) TOF gain as a function of activity concentration in a 35 cm diameter by 11.5 cm long uniform cylinder measured on the Super PETT I (SPI) scanner *(5)*. Figure reprinted with permission from *(28)*.

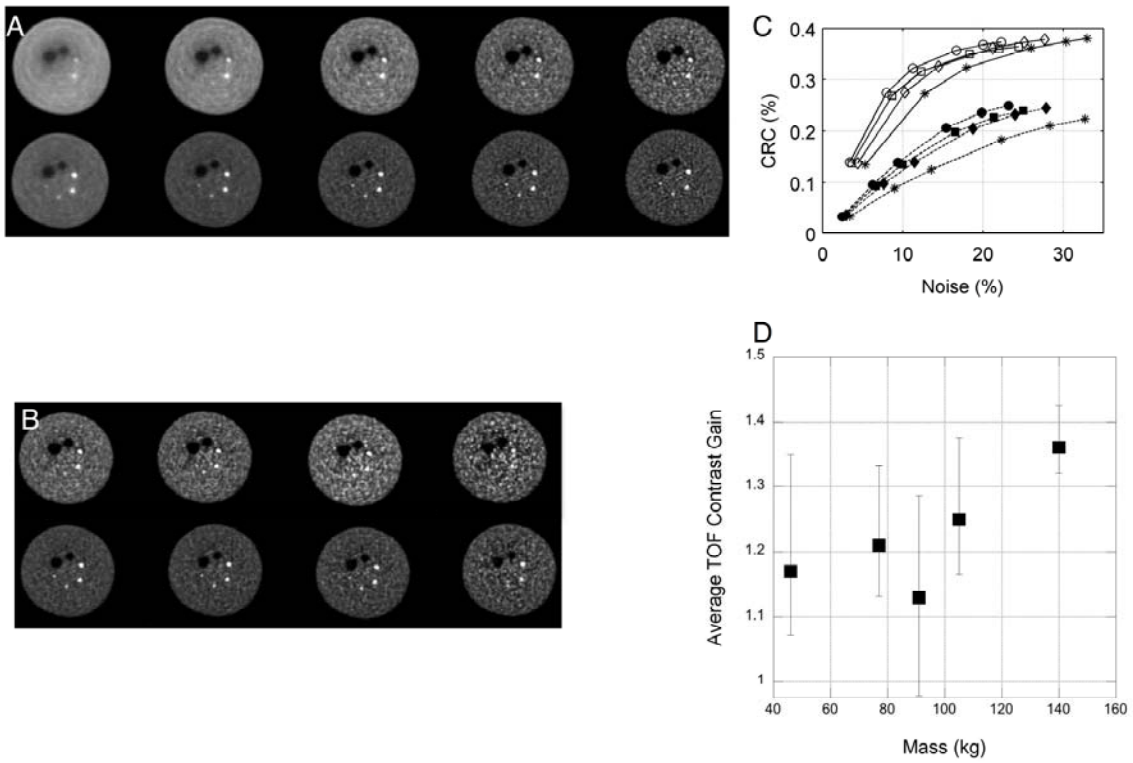

Figure 3. (A) Reconstructed Non-TOF (top row) and TOF (bottom row) images for a 35 cm diameter cylindrical lesion phantom for iteration numbers (left to right) 1, 2, 5, 10, and 20. The phantom has hot spheres (diameters of 22, 17, 13, and 10 mm) with 6:1 uptake relative to background and two cold spheres (37 and 28 mm). (B) Non-TOF (top row) and TOF (bottom row) images for the 35 cm diameter cylindrical lesion phantom for scan times of (left to right) 5, 3, 2, and 1 min. Non-TOF and TOF images are shown for iteration numbers 10 and 5, respectively where the lesion CRC values are at or close to convergence. (C) CRC for the 13 mm diameter sphere plotted as a function of image noise and plotted at iteration numbers 1, 2, 5, 10, 15, and 20. Closed symbols are for Non-TOF and open symbols are for TOF images with scan times of 2 (σ), 3 (υ), 4 (ν), and 5 (λ) mins. (D) Gain in lesion contrast as measured over several lesions in five different patients. TOF and Non-TOF images were chosen for a fixed number of iterations in order to achieve similar pixel-to-pixel noise in the images. All figures reprinted with permission from *(33)*.

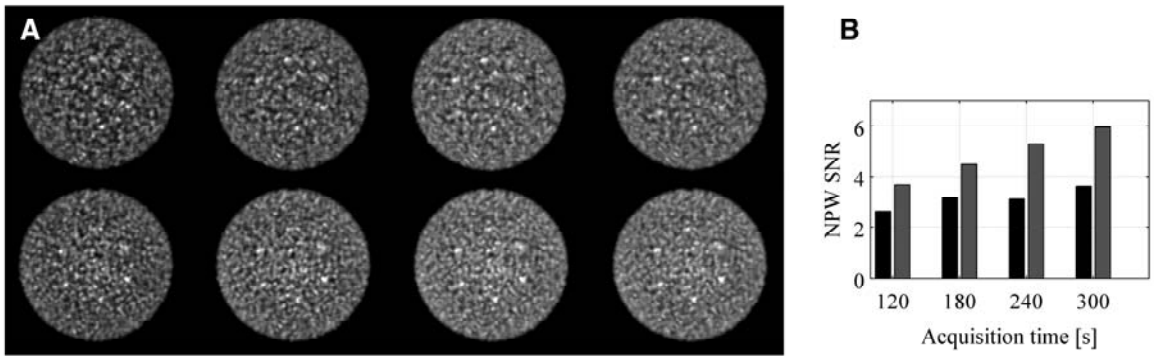

Figure 4. (A) Reconstructed Non-TOF (top row) and TOF (bottom row) images for a 35 cm diameter lesion phantom containing six, 10 mm diameter spheres with 6:1 uptake relative to the background. All images are shown after 20 iterations and are for scan times of (left to right) 1, 2, 3, 4, and 5 mins. (B) TOF gain as a function of activity concentration in a 35 cm diameter by 11.5 cm long uniform cylinder measured on the Super PETT I (SPI) scanner *(5)*. Figure reprinted with permission from *(17)*.

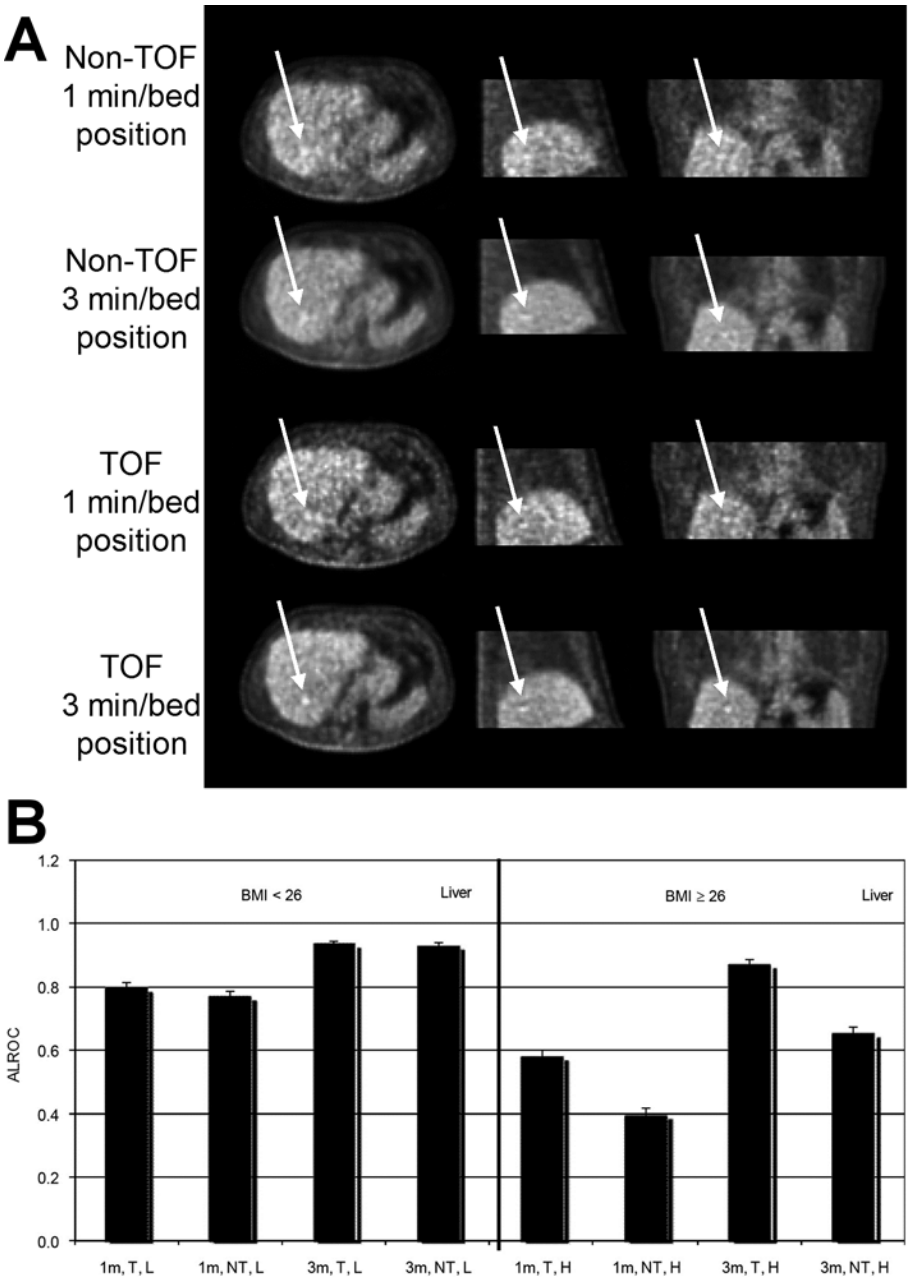

Figure 5. (A) Reconstructed images for a patient study showing a lesion synthetically inserted in the liver. Arrows indicate the location of the inserted lesion. (B) Results for average ALROC values for liver lesions shown as a function of: BMI (labels of L for BMI < 26 and H for BMI ≥ 26), scan time (labels of 1m or 3m for scan times of 1 min and 3 min, respectively), and image reconstruction (labels of NT for Non-TOF and T for TOF). All figures reprinted with permission from *(41)*.

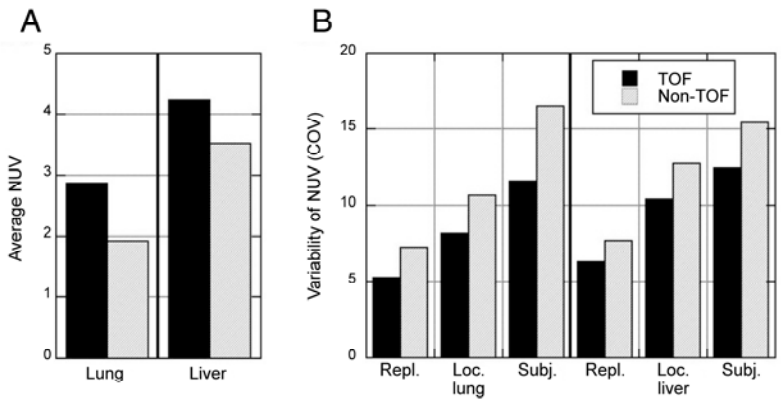

Figure 6. (A) Average sphere uptake or NUV measured in the lung and liver. (B) Variability of the sphere uptake or NUV measurement in the liver and lung shown as a function of statistical replicates (Repl.), location within the same organ (Loc.), and over different patients (Subj.). Figures reprinted with permission from *(43)*.

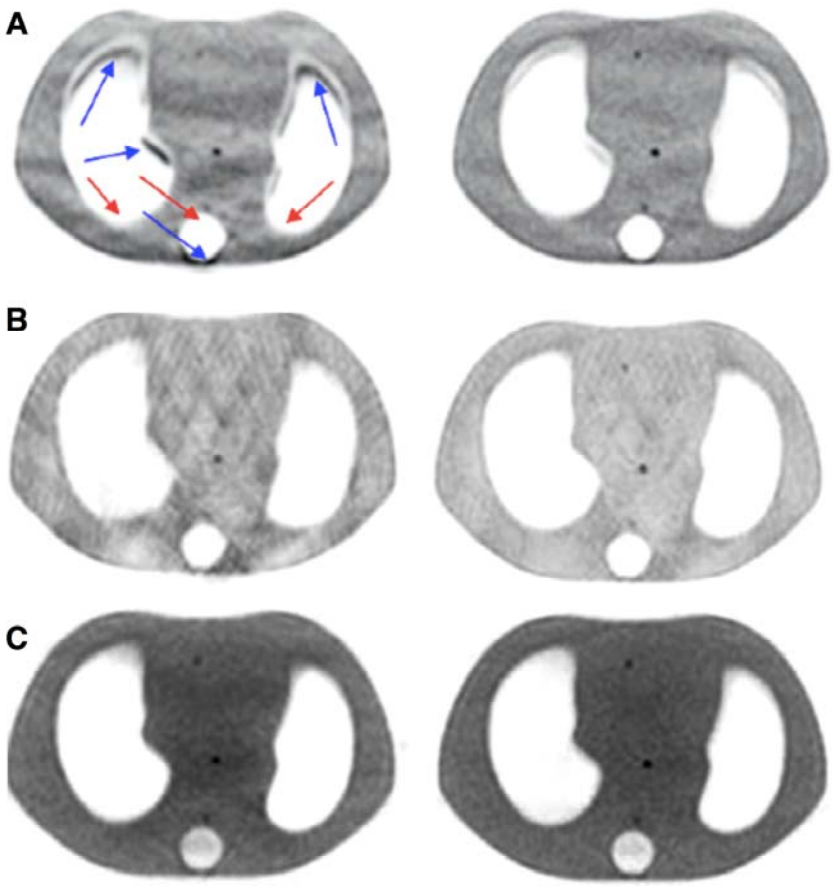

Figure 7. (A) Transverse Non-TOF (left) and TOF (right) images of a thorax phantom with a shifted attenuation correction map applied to the data. The arrows in the Non-TOF image show areas of incorrect increased and decreased counts, leading to artifacts in the image. (B) Transverse Non-TOF (left) and TOF (right) images of a thorax phantom with an incorrect normalization applied to the data. The three hot lesions are not all visible in the Non-TOF image which also shows increased artifacts. (C) Transverse Non-TOF (left) and TOF (right) images of a thorax phantom with no scatter correction applied to the data. Figures reprinted with permission from *(46)*.